Excitonic response of AA′ and AB stacked hBN bilayers

J. C. G. Henriques [1], B. Amorim [1], R. M. Ribeiro,[1,2] and N. M. R. Peres [1,2]

[1]*Department and Centre of Physics, University of Minho, Campus of Gualtar, 4710-057 Braga, Portugal*
[2]*International Iberian Nanotechnology Laboratory (INL), Avenida Mestre Jose Veiga, 4715-330 Braga, Portugal*

In this paper, we discuss the optical response due to the excitonic effect of two types of hBN bilayers: AB and AA′. Understanding the properties of these bilayers is of great utility to the study of twisted bilayers at arbitrary angles since these two configurations correspond to the limit cases of $0°$ and $60°$ rotation. To obtain the excitonic response, we present a method to solve a four-band Bethe-Salpeter equation by casting it into a one-dimensional problem, thus greatly reducing the numerical burden of the calculation when compared with strictly two-dimensional methods. We find results in good agreement with *ab initio* calculations already published in the literature for the AA′ bilayer, and predict the excitonic conductivity of the AB bilayer, which remains largely unstudied. The main difference in the conductivity of these two types of bilayers is the appearance of a small, yet well-resolved resonance between two larger ones in the AB configuration. This resonance is due to a mainly interlayer exciton, and is absent in the AA′ bilayer. Also, the conductivity of the AB bilayer is due to both intralayer and interlayer excitons and is dominated by *p*-states, while intralayer *s*-states are the relevant ones for the AA′ configuration, like in a monolayer. The effect of introducing a bias in the AA′ bilayer is also discussed.

I. INTRODUCTION

In its monolayer form, hexagonal boron nitride (hBN) is an insulator with a direct band gap located at the vertices of the first Brillouin zone, with a magnitude close to 6 eV [1]. Contrary to transition metal dichalcogenides (TMDs) [2], the lack of heavy metals leads to a rather small spin-orbit-coupling effect. The simplicity of its band structure and the large band gap make this an excellent material for the exploration of fundamental physics. Due to its structural similarity with graphene, hBN monolayers are often used as a substrate for graphene [3–5] or to encapsulate other materials, protecting them from the environment [6]. On their own, hBN monolayers are mostly studied because of their optical response dominated by excitonic resonances. In the simplest possible picture, an exciton is formed when an electron is promoted to the conduction band, leaving a hole in the valence band. These two particles, having opposite charges, interact via an electrostatic potential [7], leading to the formation of a bound state. This composite quasiparticle is then responsible for the optical absorption inside the band gap of the material. This optical response has been essential for the exploration of hBN in deep-UV optoelectronics [1,8,9].

The description of the excitonic effect deviates significantly from the single-particle response since, to capture the physics of excitons, many-body effects have to be accounted for; this is usually achieved by solving the Bethe-Salpeter equation (BSE). This integral equation in momentum space is composed of a kinetic term (obtained from the single-particle response) and an interaction term, which, in general, couples the electronic degrees of freedom of all the bands of the system via an electrostatic potential. For the case of an hBN monolayer (or monolayer TMDs for the same matter), one

can simplify the problem by considering just a single pair of bands, which couple more efficiently than the remaining ones. This version of the BSE can then be solved using many methods, with different degrees of numerical complexity, ranging from fully numerical calculations [10–13] to semianalytical [14,15] and variational [16–18] approaches.

A natural extension to the case of a single hBN monolayer is to consider the case of bilayers [19]. The ground-state configuration for this type of system is the AA′ bilayer [20,21], where the two monolayers are perfectly aligned along the stacking direction, but the boron and nitrogen atoms sit on opposite sites in the two planes. Another relevant type of bilayer, with a stability capable of competing with the AA′ configuration, is the AB bilayer, where two monolayers are shifted relative to each other. Contrary to the monolayers, both of these bilayers present a band gap with an indirect nature [21], located between the K point in the valence band and the midway point between the K and K' points in the conduction band.

Another important aspect regarding the AB and AA′ bilayers is that one configuration can be obtained from the other by a rotation of $60°$ between the constituent monolayers, making them the limiting cases of a $0°$ and $60°$ rotation in the study of twisted bilayers. Although the first theoretical studies on bilayers date back to the time when graphene was first isolated [22,23], interest in the topic only grew since then, remaining an active field of research at the time of writing [24–26]. Hence, understanding the optical response of these two configurations is of great utility to the study of arbitrary twist angles.

Contrary to the case of hBN monolayers, solving the BSE for the bilayers is a rather complex process. In fact, this is

the reason why in the current literature this type of problem is almost exclusively treated with sophisticated numerical approaches [27–31]. Although accurate, these procedures are numerically complex and require huge computational power. It is clear, then, that a simpler approach to describe these systems is needed. This is precisely the motivation behind the current paper, where we study two types of hBN bilayers, while presenting a simpler method to study the excitonic physics in this type of system, with little computational effort. Even though the excitonic response of the AA′ bilayer has already been studied in the literature, the AB bilayer remains largely unexplored.

The text is organized as follows. In Sec. II, we consider the case of the AB bilayer, with its study separated into three stages: first, we study the electronic band structure with a tight-binding model; then, we introduce the Bethe-Salpeter equation and discuss how it can be solved in order to obtain the exciton energies and wave functions; finally, we combine the results of the two previous stages and evaluate the longitudinal conductivity of the AB configuration due to excitonic resonances. In Sec. III, a similar analysis is carried out for the AA′ bilayer, where the effect of bias is also discussed. The comparison between the studied configurations is given in Sec. IV, where an overview of the work is also presented. A set of three appendices closes the paper: the first gives details of the density functional theory (DFT) calculations, the second focuses on the discussion of the excitonic angular quantum number, and the last one describes how to numerically solve the one-dimensional (1D) version of the Bethe-Salpeter equation.

II. AB BILAYER

As a starting point to the problem of the excitonic properties of hBN bilayers, we shall begin by discussing the case of the AB (or Bernal) configuration. In this type of bilayer, one finds that the two monolayers are shifted relative to each other along the armchair direction, as depicted in Fig. 1.

The first part of our study will be dedicated to the band structure of such a system, which we will describe using a tight-binding Hamiltonian and a low-energy approximation. Afterwards, the equation that governs the excitonic problem will be introduced and a simple approach to solving it will be presented. At last, the longitudinal conductivity due to excitons will be evaluated and its main features analyzed.

A. Tight-binding model

To characterize the single-particle bands of the AB bilayer, let us start by constructing a minimal tight-binding Hamiltonian directly in momentum space. In our minimal model, we account only for nearest-neighbor hoppings, both in the in-plane and out-of-plane directions; the effect of additional hopping parameters is discussed later in the text. Following the notation established in Fig. 1, we consider the basis $\{|1, b\rangle, |2, b\rangle, |2, t\rangle, |1, t\rangle\}$, where 1 and 2 refer to the sublattices (containing boron and nitrogen atoms, respectively), and b/t denotes the bottom/top layer, and find the following
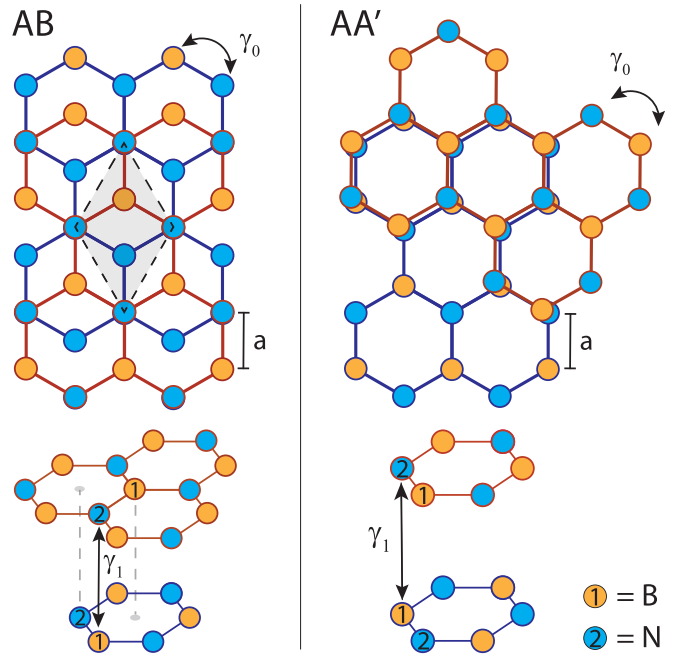

FIG. 1. Schematic representation of the lattice of AB and AA′ hBN bilayers. The nearest-neighbor in-plane and out-of-plane hoppings are γ_0 and γ_1, respectively. The nearest-neighbor distance is a.

Hamiltonian in momentum space:

$$H_{\text{TB},\mathbf{p}}^{AB} = \begin{bmatrix} E_{1,b} & \gamma_0\phi(\mathbf{p}) & \gamma_1 & 0 \\ \gamma_0\phi^*(\mathbf{p}) & E_{2,b} & 0 & 0 \\ \gamma_1 & 0 & E_{2,t} & \gamma_0\phi^*(\mathbf{p}) \\ 0 & 0 & \gamma_0\phi(\mathbf{p}) & E_{1,t} \end{bmatrix}, \quad (1)$$

where $E_{i,\lambda}$ is the on-site energy of the atom i of the λ layer, γ_0 is the hopping parameter between nearest neighbors in each monolayer, γ_1 is the interlayer hopping connecting atoms which are vertically aligned, and $\phi(\mathbf{p}) = e^{iap_y} + e^{-ia(p_x\sqrt{3}+p_y)/2} + e^{ia(p_x\sqrt{3}-p_y)/2}$ is a factor which follows from the geometrical configuration of the lattice, where a is the nearest-neighbor distance. Noting that for the AB configuration we have $E_{1,b} = E_{1,t}$ and $E_{2,b} = E_{2,t}$, we define $E_{1,b} = E_g/2 = -E_{2,b}$ to fix the zero of energy. The $|1, b/t\rangle$ and $|2, b/t\rangle$ sublattices contain boron and nitrogen atoms, respectively. To obtain the values of the different parameters, we fit the energy spectrum of this Hamiltonian to DFT calculations, the details of which we give in Appendix A, where we also show the tight-binding bands fitted to the *ab initio* results. Doing so, we find $E_g = 4.585$ eV, $\gamma_0 = 2.502$ eV, and $\gamma_1 = 0.892$ eV. It is well known that the most common functionals used in DFT underestimate the fundamental band gap, which can be corrected using advanced functionals or GW calculations. This type of approach, however, is beyond the scope of our work. When the excitonic problem is treated, we simply consider the corrected band gap to be $E_g = 6.9$ eV, where the band gap correction of [29] was considered (note that even if the correction to the band gap differs from the one used here, it should not impact the qualitative nature of the results, and even their quantitative nature should not be drastically changed). If the limit $\gamma_1 \to 0$ is considered, we recover a
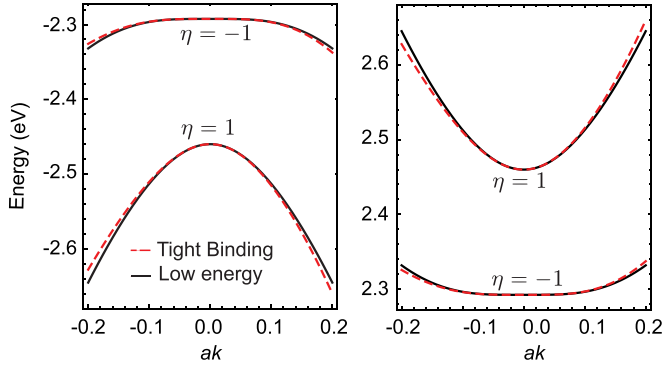
FIG. 2. Valence and conduction bands obtained from the tight-binding Hamiltonian, and the low-energy approximation for the AB bilayer. The momenta is measured relative to the K point (the results near the K' point are identical). The results obtained from the two approaches are in total agreement.

block diagonal Hamiltonian, where each block describes the electronic properties of a single hBN monolayer, as expected.

Since we will be mostly interested in the low-energy optical response, we restrict our analysis to the Dirac valleys, that is, the region around the vertices of the first Brillouin zone (1BZ), also known as the K/K' points. To do this, we write $\mathbf{p} = \tau\mathbf{K} + \mathbf{k}$ and approximate $\phi(\tau\mathbf{K} + \mathbf{k})$ to first order in $\mathbf{k}$ as $\phi_\tau(\mathbf{k}) \approx -\frac{3}{2}a(\tau k_x - ik_y)$, with $\tau = \pm 1$ labeling the K/K' points, respectively. Notice that, hereinafter, the values of $\mathbf{k} = (k_x, k_y)$ are measured relatively to these points in the reciprocal space. With this approximation, one finds the following low-energy Hamiltonian:

$$
H_{\text{low},\mathbf{k}}^{AB} = \sigma_+ \otimes \left[\hbar v_F(\tau k_x \sigma_x + k_y \sigma_y) + \frac{E_g}{2}\sigma_z \right]
$$
$$
+ \sigma_- \otimes \left[\hbar v_F(\tau k_x \sigma_x - k_y \sigma_y) - \frac{E_g}{2}\sigma_z \right]
$$
$$
+ \sigma_x \otimes \sigma_+ \gamma_1, \tag{2}
$$

where $\sigma_\pm = (I \pm \sigma_z)/2$ and $\hbar v_F = 3\gamma_0 a/2$. Diagonalizing this Hamiltonian we find the energy dispersion relations,

$$
E_{\mathbf{k}}^{\lambda,\eta} = \frac{\lambda}{2}\sqrt{E_g^2 + 4\hbar^2 v_F^2 k^2 + 2\gamma_1^2 + 2\gamma_1\eta\Lambda_{\mathbf{k}}}, \tag{3}
$$

with $\Lambda_{\mathbf{k}} = \sqrt{\gamma_1^2 + 4\hbar^2 v_F^2 k^2}$, $\lambda = \pm 1$ (when used as a number) or $\lambda = c/v$ (when used as an index), and $\eta = \pm 1$. Just like in the case of an hBN monolayer, the energy spectrum is the same for $\tau = 1$ or $\tau = -1$ since we ignore the small effect of spin-orbit coupling in this system. In Fig. 2, we depict the band structure obtained from the tight-binding model as well as from the low-energy approximation in the vicinity of the Dirac points; the agreement between the two results is clear, as it should be. Moreover, we find that the bands associated with the index $\eta = +1$ take an approximately parabolic shape, while those with $\eta = -1$ present a momentum dependence proportional to k^4. A similar band structure is found on bilayer

TMDs, such as $3R - MoS^2$ [32]. The eigenvectors associated with each band read

$$
|u_{\mathbf{k}}^{v,\tau,\eta}\rangle = \frac{1}{\sqrt{\mathcal{V}_{\eta,\mathbf{k}}}}
\begin{bmatrix}
\tau e^{\tau i\theta}\frac{\gamma_1 + \eta\Lambda_{\mathbf{k}}}{2\hbar v_F k} \\
e^{2\tau i\theta}\frac{\left(E_g - 2E_{\mathbf{k}}^{v,\eta}\right)(\gamma_1 - \eta\Lambda_{\mathbf{k}})}{4k^2\hbar^2 v_F^2} \\
-\tau e^{\tau i\theta}\frac{E_g - 2E_{\mathbf{k}}^{v,\eta}}{2\hbar v_F k} \\
1
\end{bmatrix}, \tag{4}
$$

$$
|u_{\mathbf{k}}^{c,\tau,\eta}\rangle = \frac{1}{\sqrt{\mathcal{C}_{\eta,\mathbf{k}}}}
\begin{bmatrix}
\tau e^{\tau i\theta}\frac{\gamma_1 + \eta\Lambda_{\mathbf{k}}}{2\hbar v_F k} \\
e^{2\tau i\theta}\frac{\left(E_g - 2E_{\mathbf{k}}^{c,\eta}\right)(\gamma_1 - \eta\Lambda_{\mathbf{k}})}{4k^2\hbar^2 v_F^2} \\
-\tau e^{\tau i\theta}\frac{E_g - 2E_{\mathbf{k}}^{c,\eta}}{2\hbar v_F k} \\
1
\end{bmatrix}, \tag{5}
$$

where $\mathcal{C}_{\eta,\mathbf{k}}/\mathcal{V}_{\eta,\mathbf{k}}$ are normalization factors and $\theta = \arctan(k_y/k_x)$. Just like for any other state vector, these spinors are defined up to a global phase factor (for example, $e^{\tau i\theta}$). The particular choice used in (5) was made in order to simplify the numerical formulation of the excitonic problem, which will be discussed in the following section. At last, let us note for future reference that for small momentum, these vectors take the approximate form

$$
|u_{\mathbf{k}}^{v,-}\rangle \approx
\begin{bmatrix}
0 \\
e^{2\tau i\theta} \\
0 \\
0
\end{bmatrix}, \qquad
|u_{\mathbf{k}}^{v,+}\rangle \approx
\begin{bmatrix}
e^{i\tau\theta}\sin\frac{\xi}{2} \\
0 \\
-e^{i\tau\theta}\cos\frac{\xi}{2} \\
0
\end{bmatrix}, \tag{6}
$$

$$
|u_{\mathbf{k}}^{c,-}\rangle, \approx
\begin{bmatrix}
0 \\
0 \\
0 \\
1
\end{bmatrix}, \qquad
|u_{\mathbf{k}}^{c,+}\rangle \approx
\begin{bmatrix}
e^{i\tau\theta}\cos\frac{\xi}{2} \\
0 \\
e^{i\tau\theta}\sin\frac{\xi}{2} \\
0
\end{bmatrix}, \tag{7}
$$

with $\xi = \arctan[2\gamma_1/E_g]$.

B. Excitonic problem

Now that the single-particle bands and Bloch factors were determined, let us tackle the problem of obtaining the excitonic energies and wave functions.

To obtain the energies and wave functions of the excitons in the AB bilayer, we shall solve the well-known Bethe-Salpeter equation (BSE). The BSE is an integral equation in momentum space, which requires the information of the single-particle approximation and whose solution determines the excitonic spectrum. Explicitly, for an exciton with zero center of mass momentum, this equation reads [14,33,34]

$$
\left(E_{\mathbf{k}}^c - E_{\mathbf{k}}^v\right)\psi_{cv}(\mathbf{k}) - \sum_{\mathbf{q}c'v'} V(\mathbf{k} - \mathbf{q})\langle u_{\mathbf{k}}^c|u_{\mathbf{q}}^{c'}\rangle\langle u_{\mathbf{q}}^{v'}|u_{\mathbf{k}}^v\rangle
$$
$$
\times \psi_{c'v'}(\mathbf{q}) = E\psi_{cv}(\mathbf{k}), \tag{8}
$$

where, for the sake of a simpler notation, we have omitted the indexes τ and η, which are now included in the band index (c/c' or v/v'). Here, the sum is performed over the momentum $\mathbf{q}$ and all the bands of our model, $\psi_{cv}(\mathbf{k})$ refers to the exciton's wave function projected onto the pair of bands (v, c), E corresponds to the exciton's energy, and $V(\mathbf{k} - \mathbf{q})$ is the Fourier transform of the electron-hole interaction, which we model with the Rytova-Keldysh potential [7,35,36]. This potential can be obtained from the solution of the Poisson equation for a charge embedded in a thin film and is known to accurately

capture the electrostatic interaction in 2D materials. It reads

$$V(\mathbf{k}) = \frac{2\pi\hbar c\alpha}{\epsilon k(1 + r_0 k)}, \tag{9}$$

with c the speed of light, $\alpha \sim 1/137$ the fine-structure constant, ϵ the mean dielectric constant of the media above and below the monolayer, and r_0 an in-plane screening length, which is related with the 2D polarizability of the system [37]. In the interacting part of Eq. (8), we considered only the direct electron-hole interaction and neglected the exchange contribution, following Ref. [34], where it was shown that such a contribution introduces only minute corrections on the exciton's binding energies (smaller than 5%). We now note that Eq. (8) corresponds, in fact, to a set of four coupled equations, one for each pair of valence and conduction bands (v, c), defining an eigenvalue problem. In this type of system, the formation of an exciton cannot be *a priori* assigned to a single pair of bands, but rather to a cooperative process where the four bands of the model contribute to the formation of such an entity. Furthermore, from Eq. (8), one already sees that the phases chosen for the Bloch factors in Eq. (5) have an impact on the BSE since different phase choices lead to different angular dependencies for the term $\langle u_{\mathbf{k}}^c | u_{\mathbf{q}}^{c'} \rangle \langle u_{\mathbf{q}}^{v'} | u_{\mathbf{k}}^v \rangle$. We stress, however, that when a physical quantity is computed, for example a conductivity, its final result is independent from the phase that one initially chose for the Bloch factors.

Solving the BSE is no simple task and, as mentioned in Sec. I, different techniques are frequently employed to achieve this. The approach we consider here is to use the results of the tight-binding model that we previously presented, and reduce the BSE to a 1D integral equation, which can then be easily solved with a single numerical quadrature. In what follows, we give a brief description of the approach we use, with a more detailed technical discussion presented in Appendix C.

The first step to transform the BSE into a 1D integral equation is to consider the system to be isotropic, which allows us to write the exciton's wave function as the product of a radial component and an angular component, such as $\psi_{cv}(\mathbf{k}) = f_{cv}(k)e^{im\theta_k}$, with m an integer. At first, one might be tempted to associate the value of m with the angular momentum of the exciton; however, this is not necessarily true. From the study of hBN monolayers (or other systems which can be treated with a two-band model), it is known that the number which characterizes the angular momentum is obtained from a combination of the m present in the envelop function $\psi_{cv}(\mathbf{k})$ with an additional contribution stemming from the pseudospin of the system [38,39]. However, for a model with four bands (such as the one we currently consider), the identification of the pseudospin contribution is unclear and, because of that, we will refrain from attributing an angular quantum number to excitons that appear from the solution of the BSE when the four bands are accounted for. In Appendix B, we give a more detailed discussion of this. We note in passing that the presented approach may be applied to other multilayer systems.

Making use of the above-mentioned proposal for the wave function $\psi_{cv}(\mathbf{k}) = f_{cv}(k)e^{im\theta_k}$, the BSE acquires the form

$$\left(E_k^c - E_k^v\right)f_{cv}(k) - \sum_{c'v'}\int qdqd\theta_q V(\mathbf{k} - \mathbf{q})\langle u_{\mathbf{k}}^c | u_{\mathbf{q}}^{c'}\rangle\langle u_{\mathbf{q}}^{v'} | u_{\mathbf{k}}^v\rangle$$

$$\times f_{c'v'}(q)e^{im(\theta_q - \theta_k)} = Ef_{cv}(k). \tag{10}$$

We now note that according to Eq. (9), $V(\mathbf{k} - \mathbf{q})$ is a function of k, q, and $\cos(\theta_q - \theta_k)$, that is, $V(\mathbf{k} - \mathbf{q}) \equiv V(k, q, \theta_q - \theta_k)$. Knowing this, one easily sees that if the angular dependence of the spinor product $\langle u_{\mathbf{k}}^c | u_{\mathbf{q}}^{c'}\rangle\langle u_{\mathbf{q}}^{v'} | u_{\mathbf{k}}^v\rangle$ only contains terms of the form $e^{in(\theta_q - \theta_k)}$, with n a real number, then the integral over $d\theta_q$ can be converted into an integral over a new variable $\vartheta = \theta_q - \theta_k$, independent of q and k. By removing the momentum dependence from the angular integral, its evaluation can be thought of as an independent step of the calculation, thus effectively transforming the BSE into a 1D integral equation (whose only integration variable is now q), which can then be easily solved (see Appendix C). This approach is computationally advantageous when compared with a strictly two-dimensional calculation (which scales as N^4, while the simpler 1D problem scales as N^2, with N the number of points in the numerical quadrature). For clarity, we note that the method we described to solve the BSE is based on the low-energy approximation near the Dirac points, which allowed us to write the momentum integral as we did, instead of solving the integral equation over the entire Brillouin zone.

The key point now is to find the spinor's phase choice which guarantees that their product has the desired angular dependence. First, we note that for the term $\langle u_{\mathbf{k}}^c | u_{\mathbf{q}}^{c'}\rangle\langle u_{\mathbf{q}}^{v'} | u_{\mathbf{k}}^v\rangle$ with $c = c'$ and $v = v'$, the angular dependence always presents the form we are seeking, regardless of the phase choice, since the phase of each $|\text{ket}\rangle$ is balanced by the phase of the $\langle\text{bra}|$ with which it is contracted. This is precisely what one finds in the case of monolayers, where the BSE can consistently be transformed into a 1D integral equation [14]. What about the remaining terms where $c \neq c'$ and/or $v \neq v'$? Depending on the phase choice for the spinors, one may find that unwanted terms, such as $e^{in\theta_q}e^{-ip\theta_k}$, with $p \neq n$, appear. Using Eq. (5), however, produces the desired angular dependence for all the products of spinors that appear in the BSE, thus allowing us to convert the excitonic problem into a 1D integral equation.

Using the method we have just highlighted, and discuss in more detail in Appendix C, we solved the BSE for the AB bilayer for different values of m (which, we recall, does not correspond directly to the angular quantum number). We considered the bilayer to be suspended, $\epsilon = 1$, and used $r_0 = 16$ Å, in agreement with the value found from *ab initio* calculations in [29]. When solving the BSE, we employed a Gauss-Legendre quadrature, containing 100 points, which we verified to be more than enough to guarantee the convergence of the energies and wave functions for the first 10 excitonic states.

In Figs. 3(a)–3(c), we depict the wave functions, $|\Psi(k)|^2 = \sum_{cv}|\psi_{cv}(k)|^2$, associated with three of the states found from the solution of the BSE. These states are some of the most relevant ones for the linear optical response of the system (computed in the following section), and their energies read $E_{n=1} = 5.71$ eV, $E_{n=2} = 6.13$ eV, and $E_{n=3} = 6.34$ eV. Analyzing the three panels, we see that the $n = 1$ and $n = 3$ states present wave functions which are similar to those found in the bound states of the 2D hydrogen atom [40] (which, in turn, are similar to those of its three-dimensional counterpart). In fact, since these wave functions are zero at the origin, have an approximately linear behavior for small momentum, and present zero and one nodes, respectively, they bear a particular resemblance to the $2p$ and $3p$ states of the hydrogen atom. At
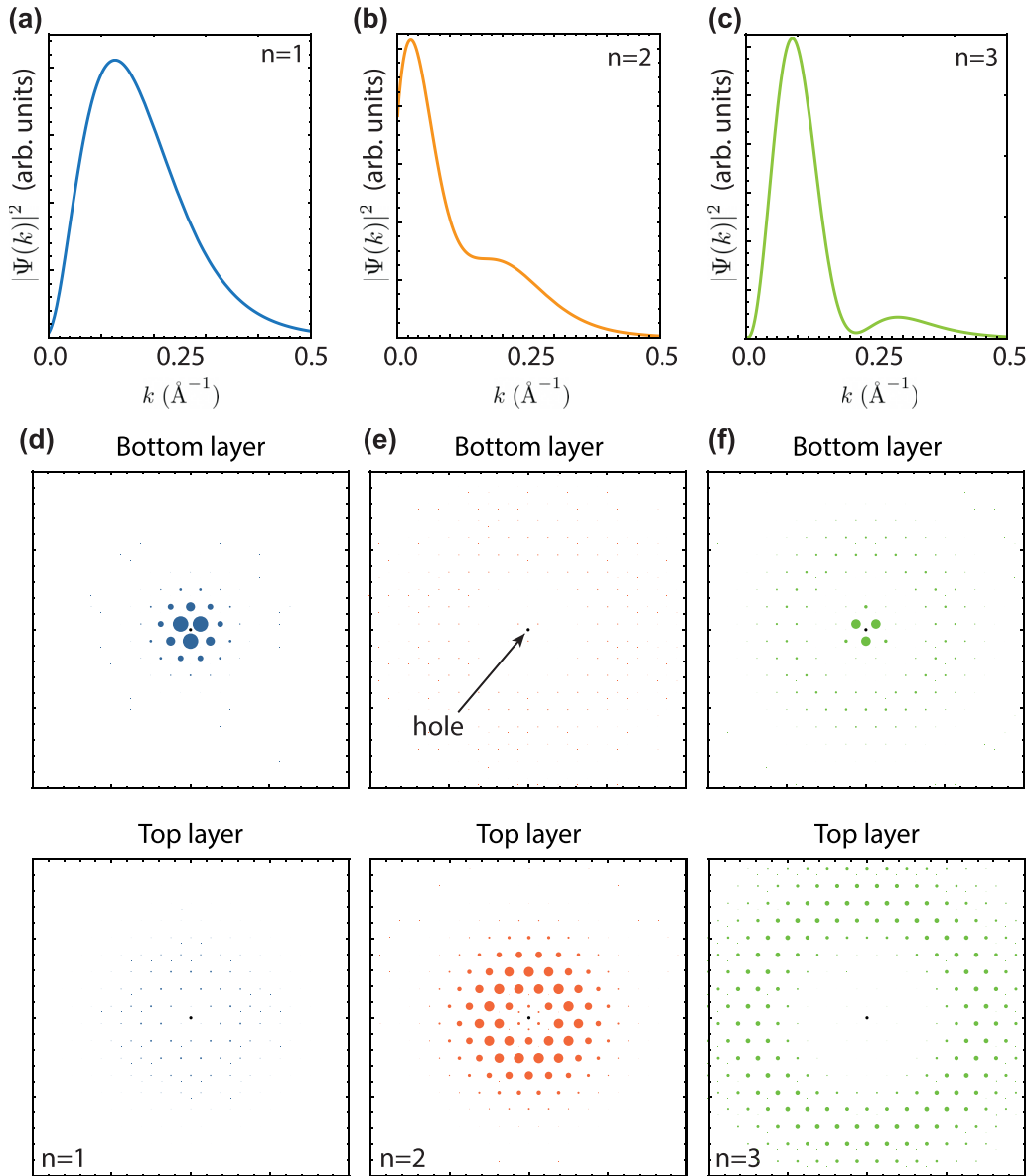
FIG. 3. (a)–(c) Wave functions in momentum space, $|\Psi(k)|^2 = \sum_{cv} |\psi_{cv}(k)|^2$, of the three excitonic states which are responsible for the first three resonances of the optical conductivity. Their energies are $E_{n=1} = 5.71$ eV, $E_{n=2} = 6.13$ eV, and $E_{n=3} = 6.34$ eV. (d)–(f) Real-space representation of the absolute value of the wave function in both layers when the hole is placed on the nitrogen site of the bottom layer ($|2, b\rangle$ sublattice).

odds with this, the wave function of the $n = 2$ state presents a more exotic behavior, with a broad shoulder instead of a node, unlike a hydrogenic wave function.

To gain more information about these states, especially regarding their configuration in real space, we compute the projection of their wave functions onto the electron and hole sublattices, which can be written as

$$\Psi_{\alpha\beta}(\mathbf{r}_e, \mathbf{r}_h) = \sum_{\mathbf{k},c,v} e^{i(\mathbf{K}+\mathbf{k})\cdot(\mathbf{r}_e-\mathbf{r}_h)} \psi_{cv}(\mathbf{k}) u_{\mathbf{k},c}^{\alpha} \left(u_{\mathbf{k},v}^{\beta}\right)^*, \quad (11)$$

where $\mathbf{r}_e$ and $\mathbf{r}_h$ are the electron and hole positions, respectively, and $u_{\mathbf{k},c}^{\alpha}$ refers to the α sublattice entry of the Bloch factor $|u_{\mathbf{k},c}\rangle$ (an analogous definition holds for $u_{\mathbf{k},v}^{\beta}$). For simplicity, we consider $\mathbf{r}_h = 0$ and study the behavior of

the wave function with $\mathbf{r}_e$. Notice how the the term $\mathbf{K} + \mathbf{k}$ appears on the complex exponential because the momenta are being measured relative to the Dirac point; however, the contribution from $\mathbf{K}$ vanishes when the square modulus of the wave function is considered. In Figs. 3(d)–3(f), we depict the real-space wave functions when the hole is placed on the nitrogen atom of the bottom layer ($|2, b\rangle$); the position of the hole is marked by a small black dot in the center of each figure. For the $n = 1$ exciton, we find that the wave function is mainly distributed on the bottom layer boron sites (this is the reason we apparently only see a triangular lattice, instead of a honeycomb one), that is, on the same layer as the hole, with a smaller portion being present on the top layer; this distribution of the wave function indicates that

TABLE I. Integrate values of the square modulus of the sublattice resolved real-space wave function for the AB bilayer. The horizontal top row indicates the sublattice where the hole is placed, while the two columns on the left indicate the exciton we are considering, and the layer where the electron is located.

		$\lvert 1,b\rangle$	$\lvert 2,b\rangle$	$\lvert 2,t\rangle$	$\lvert 1,t\rangle$
$n=1$	Bottom	0.01	0.34	0.03	0.00
	Top	0,00	0.26	0.34	0.01
$n=2$	Bottom	0.00	0.17	0.01	0.00
	Top	0.02	0.61	0.17	0.01
$n=3$	Bottom	0.01	0.17	0.08	0.00
	Top	0.00	0.57	0.16	0.01

this state has a predominantly intralayer nature. On the other hand, for the $n=2$ and $n=3$ excitons, we find a rather significant part of the wave function spread over the top layer, indicating the interlayer character of these excitations. To more easily understand how the wave function behaves for different positions of the hole, we present, in Table I, the values found for the integrated square modulus of the wave function, $\int |\Psi_{\alpha\beta}(\mathbf{r}_e,0)|^2 d\mathbf{r}_e$, which gives the probability of finding the electron on one of the layers, for each possible location of the hole. From the inspection of this table, one finds that (i) there is a clear preference for the hole to be located on the $\lvert 2,t/b\rangle$ sublattices (containing nitrogen atoms), given the small values found for the integrated wave function when the hole is located on either $\lvert 1,b/t\rangle$ sublattices; and (ii) we confirm the previous assignment of the $n=1$ exciton as mainly intralayer, while the $n=2$ and $n=3$ ones are mostly interlayer.

C. Optical conductivity

Now that the the BSE was solved for the AB bilayer, we are ready to evaluate its conductivity due to the excitonic effect. Following Ref. [33], we write the conductivity for a multiband system as

$$\frac{\sigma(\omega)}{\sigma_0} = \frac{i}{\pi} \sum_n E_n \frac{\mathbf{\Omega}_n \mathbf{\Omega}_n^*}{E_n - \hbar\omega} + (\omega \to -\omega)^*, \quad (12)$$

where $\sigma_0 = e^2/4\hbar$ is the conductivity of graphene, the sum over n runs over the different exciton states with energy E_n and

$$\mathbf{\Omega}_n = \sum_{vc\mathbf{k}} \psi_{cv}^{(n)}(\mathbf{k}) \mathbf{\Omega}_{vc\mathbf{k}}, \quad (13)$$

where $\mathbf{\Omega}_{vc\mathbf{k}}$ is the position operator interband matrix element, which we write as

$$\mathbf{\Omega}_{vc\mathbf{k}} = \frac{\langle u_{\mathbf{k}}^v | [H, \mathbf{r}] | u_{\mathbf{k}}^c \rangle}{E_{\mathbf{k}}^v - E_{\mathbf{k}}^c}, \quad (14)$$

with H standing for the low-energy tight-binding Hamiltonian. The evaluation of the interband matrix element is crucial to determine which of the solutions of the BSE couple with the electric field and, consequently, contribute to the conductivity. For the current system, the interband matrix elements impose that only states with $m = \pm\tau$ may give a finite contribution (we recall once more that this does not correspond to the
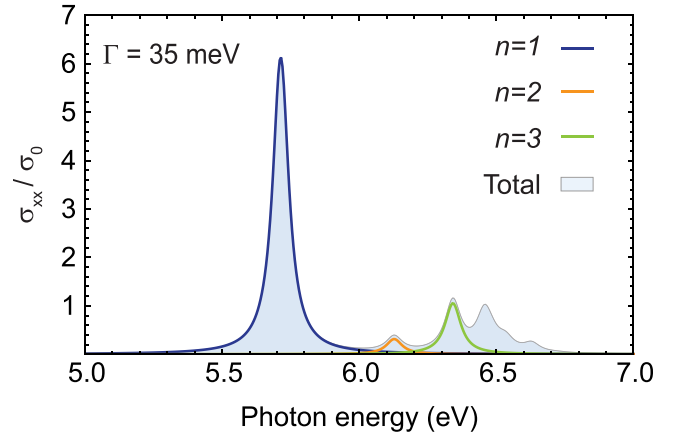

FIG. 4. Optical conductivity of an AB hBN bilayer accounting for the first 10 exciton states with $m = \tau$ (the contributions from both valleys were accounted for). The first three resonances correspond to the excitonic states depicted in Fig. 3. To obtain this result, a phenomenological broadening of 35 meV was considered. The conductivity is given in terms of the conductivity of graphene, $\sigma_0 = e^2/4\hbar$.

angular quantum number). In addition, the sum over the bands also plays a role in determining which states couple more efficiently with light due to the possibility of existing constructive or destructive interference between the different terms. Using the solutions of the BSE given in the previous section, we compute the optical response of the system due to a linearly polarized electric field; its conductivity is depicted in Fig. 4, where a phenomenological broadening of 35 meV was considered for all resonances. The shaded blue area corresponds to the conductivity accounting for 10 exciton states (all with $m = \tau$, since we found the $m = -\tau$ states to have rather small oscillator strengths); the contributions of the states highlighted in Fig. 3 are depicted in the same color as the corresponding wave functions. From this figure, we see that the longitudinal conductivity of the AB hBN bilayer has its more pronounced feature on the first resonance, while a set of lower intensity ones appear at higher energies. Furthermore, the conductivity of the AB bilayer presents a small, yet noticeable resonance between the first and third peaks, which can be ascribed to the second state of Fig. 3. Above the third resonance and up to approximately 6.5 eV, three resonances appear. These peaks, however, overlap significantly, making it difficult to resolve them. Moreover, since our model is based on a low-energy approximation, the results are expected to become progressively less accurate as we approach the band edge. For these two reasons, we focus our analysis solely on the first three resonances.

D. Exciton angular quantum number

Having determined the complete longitudinal conductivity using the results of the four-band BSE, we shall now carry out a complementary analysis to gain further insight into the nature of each resonance, especially regarding the angular quantum number of the excitons behind them.

As a first, and somewhat naive, approach, we return to the BSE and restrict it to a single pair of valence and conduc-
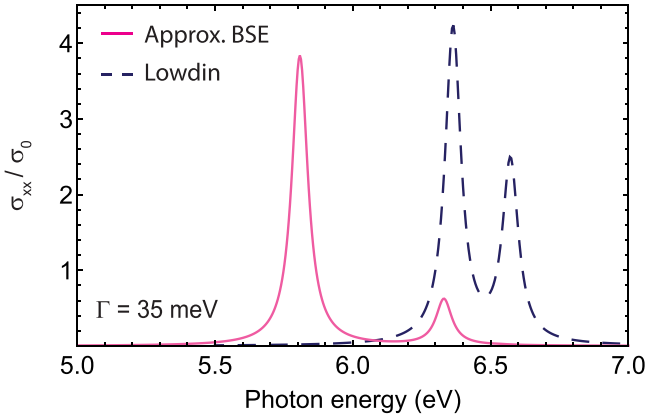
FIG. 5. Optical conductivity of an AB hBN bilayer obtained by (i) considering only two of the original four bands when solving the BSE (labeled as Approx. BSE), and (ii) using the Lowdin partitioning. As in Fig. 4, a broadening of 35 meV was introduced. The conductivities are given in terms of the conductivity of graphene, $\sigma_0 = e^2/4\hbar$.

tion bands. In particular, we consider only the bands which present an energy dispersion in k^4 since intuition tells us that these should dominate in the low-energy response. Because in this approximation we are effectively treating a two-band problem, we can identify the contribution of the pseudospin to the angular quantum number (see Appendix B).

Let us define the excitonic wave function in real space for a two-band model [38] as

$$\Psi_{\alpha,\beta}(\mathbf{r}_e, \mathbf{r}_h) = \sum_{\mathbf{k}} e^{i(\mathbf{K}+\mathbf{k})\cdot(\mathbf{r}_e-\mathbf{r}_h)} \psi_{cv}(\mathbf{k}) u_{\mathbf{k},c}^{\alpha} \left(u_{\mathbf{k},v}^{\beta}\right)^*, \quad (15)$$

which is analogous to the previously given definition, only this time without the sum over the bands since a single pair is being considered. From Eq. (7), one sees that for small momentum, the product $u_{\mathbf{k},c}^{\alpha} (u_{\mathbf{k},v}^{\beta})^*$ approximately introduces an additional phase of $e^{-2i\tau\theta}$ (recall that only the bands with $\eta = -1$ are being currently considered), which can be combined with the angular part of $\psi_{cv}(\mathbf{k})$. Hence, within this approximation, we may define the angular quantum number of the exciton as $m_X = m + m_{ps}$, where $m_{ps} = -2\tau$ is the pseudospin contribution to the angular quantum number and m is the contribution from the envelope function, $\psi_{cv}(\mathbf{k})$.

When the conductivity is evaluated, the interband matrix element imposes that only states with $m = \pm\tau$ may couple with the external excitation. Thus, taking into consideration the definition of the angular quantum number m_X, we find that at least approximately, only states with angular quantum numbers $m_X = -\tau$ or $m_X = -3\tau$ are optically bright. In analogy with the hydrogen atom, we label these states as p- and f-states since the modulus of their angular quantum number is 1 and 3, respectively. These selection rules are in line with the momentum space wave functions depicted in Fig. 3.

In Fig. 5, we depict the conductivity found with this two-band approximation, where once again a phenomenological broadening of 35 meV was considered; only the first two p-states were accounted for since the f-states appear above these two, and with a far smaller oscillator strength. Com-

paring this result with the one of Fig. 4, one clearly sees the resemblance between the two conductivities, both in the location of the resonances as well as their relative magnitude. The absolute magnitude is slightly different from what was found when the four-band BSE was solved; this is to be expected since, in the current approximation, we are neglecting the contribution of other pairs of bands to the conductivity. Thus, it appears that one can confidently assign, at least approximately, the hydrogenic labels of $2p$ and $3p$ states to the excitons which originate the first and third resonances of the conductivity in Fig. 4. Note, however, how the small resonance at approximately 6 eV in Fig. 4 is absent in this approximation. By repeating this procedure for all possible pairs of bands, we find that using the $\eta = -1$ bands gives the best results when compared with the four-band calculation. Moreover, we note that the small resonance is only ever captured when the four bands are accounted for, indicating a clear difference of this exciton when compared with the other two we are considering (which can be approximately captured by selecting two of the four bands of our model).

To further confirm the correct labeling of the resonances, we can follow the ideas of Ref. [41], where the process of folding a tight-binding Hamiltonian on itself, i.e., applying a Lowdin partitioning [42,43], was used to obtain the optical selection rules of a $3R - MoS^2$ bilayer. In a succinct manner, to obtain an effective 2×2 Hamiltonian from a given 4×4 model Hamiltonian, one should start by finding the unitary transformation which diagonalizes the model Hamiltonian at $k = 0$. Then, the unitary transformation should be applied to the model Hamiltonian with finite k, and the basis should be reordered such that the low-energy diagonal terms appear on the upper left 2×2 block. At last, the effective Hamiltonian is obtained from this one through the relation

$$(H_{\mathrm{eff}})_{ij} = \tilde{H}_{ij} + \frac{1}{2}\sum_l \frac{\tilde{H}_{il}\tilde{H}_{lj}}{H_{ii}-H_{ll}} + \frac{\tilde{H}_{il}\tilde{H}_{lj}}{H_{jj}-H_{ll}}, \quad (16)$$

with $i, j = \{1, 2\}$ and $l = \{3, 4\}$; $\tilde{H}$ corresponds to the model Hamiltonian after applying the unitary transformation and rearranging its basis. Hence, using the described procedure to project the high-energy bands onto the low-energy ones, we obtain the following effective two-band Hamiltonian:

$$H_{\mathrm{eff}} \approx \begin{pmatrix} \frac{E_g}{2} & -\frac{\hbar^2 v_F^2}{\gamma_1} k^2 e^{-2i\tau\theta} \\ -\frac{\hbar^2 v_F^2}{\gamma_1} k^2 e^{2i\tau\theta} & -\frac{E_g}{2} \end{pmatrix}. \quad (17)$$

According to Ref. [41], the winding number associated with this Hamiltonian is $w = -2\tau$; and the optical selection rules follow from the winding number as $m_X = w \pm \tau$, when trigonal warping is neglected. Thus, using this alternative approach, we once again find selection rules which only allow the excitation of states with $m_X = -\tau$ and $m_X = -3\tau$, that is, p- and f-states. If the effect of trigonal warping had been included, for example by introducing hopping to second neighbors (either in the in-plane or out-of-plane directions), the set of selection rules would be extended to include s- and d-states (with angular quantum number 0 and 2, respectively), due to an additional contribution of a factor of 3 to m_X stemming from the symmetry of the lattice. Since the resonances associated with these states would be proportional

to the square of the associated hopping integral, which is significantly smaller than the nearest-neighbor hoppings, their intensity would be rather small when compared to the resonances we have accounted for here.

At last, we note that if one now solves the excitonic problem using H_{eff} as a starting point, the exciton energies will be significantly overestimated. This is a consequence of the band structure given by H_{eff}, where the dispersion relation presents a k^4 dependence near $k \to 0$, but grows at a much faster rate than the original bands as the momentum increases. This results in a higher kinetic energy for the electrons, which in turn reduces the exciton binding energies. Hence, even though the Lowdin partitioning captures the qualitative features of the conductivity of the AB bilayer and easily gives optical selection rules, it fails to quantitatively describe its conductivity, as we show in Fig. 5.

III. AA′ BILAYER

In this section, we will focus on AA′ bilayers. In this type of bilayer, the two monolayers are vertically aligned, with the boron and nitrogen atoms in opposite sites, such that a boron/nitrogen atom is always vertically aligned with a nitrogen/boron atom. A depiction of this type of bilayer is presented in Fig. 1. As in the previous section, we will begin by studying the electronic band structure of the system followed by the calculation of the excitonic response. Since the ideas and techniques of the previous section carry on to the current one, in what follows we will give a less detailed description of how the results were obtained and will mainly focus on the differences between the two types of bilayer.

A. Tight-binding model

To obtain the low-energy band structure of the AA′ bilayer, we will once more use a tight-binding Hamiltonian written directly in momentum space. Working in the basis $\{|1, b\rangle, |2, b\rangle, |1, t\rangle, |2, t\rangle\}$ (see Fig. 1), we write

$$
H_{\text{TB},\mathbf{p}}^{AA'} = \begin{bmatrix} E_g/2 & \gamma_0 \phi^*(\mathbf{p}) & 0 & \gamma_1 \\ \gamma_0 \phi(\mathbf{p}) & -E_g/2 & \gamma_1 & 0 \\ 0 & \gamma_1 & E_g/2 & \gamma_0 \phi(\mathbf{p}) \\ \gamma_1 & 0 & \gamma_0 \phi^*(\mathbf{p}) & -E_g/2 \end{bmatrix}. \quad (18)
$$

Here we have considered $E_{1,b} = E_{1,t}$ and $E_{2,b} = E_{2,t}$, and defined E_g as $E_{1,b} = E_g/2 = -E_{2,b}$. The $|1, b/t\rangle$ and $|2, b/t\rangle$ contain boron and nitrogen atoms, respectively. As in the AB bilayer, γ_0 and γ_1 refer to the intra- and interlayer nearest-neighbor hoppings, respectively, and $\phi(\mathbf{p})$ is a phase factor whose expression is the same as in the previous section. Notice how for the AA′ bilayer, the Hamiltonian presents twice as many γ_1 as for the AB configuration, in agreement with the increased number of atoms which are vertically aligned. As before, if $\gamma_1 \to 0$, one is left with a block diagonal Hamiltonian describing two decoupled monolayers. To obtain the numerical values for the different parameters of the model, the energy spectrum of the tight-binding Hamiltonian was fitted to DFT calculations (obtained in an identical manner to what was described in the previous section), yielding $E_g = 4.65 \, \text{eV}$, $\gamma_0 = 2.491 \, \text{eV}$, and $\gamma_1 = 0.595 \, \text{eV}$.
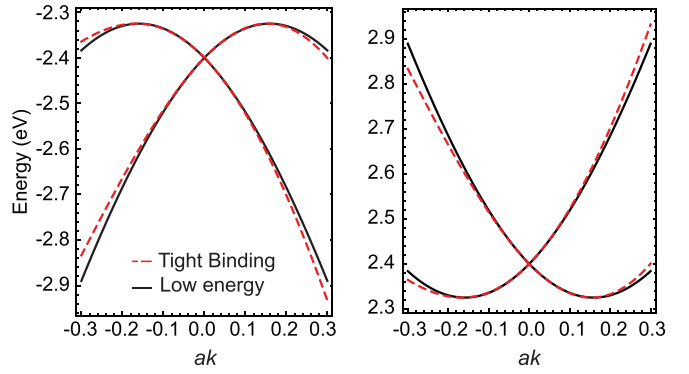

FIG. 6. Valence and conduction bands obtained from the tight-binding Hamiltonian, and the low-energy approximation for the AA′ bilayer. The momenta are measured relative to the K point (the results near the K' point are identical). A good agreement is seen between the two sets of data.

In the low-energy approximation, that is, near the Dirac points, we write $\phi_\tau(\mathbf{k}) \approx -\frac{3}{2}a(\tau k_x - i k_y)$, and find the effective low-energy Hamiltonian,

$$
H_{\text{low},\mathbf{k}}^{AA'} = \sigma_+ \otimes \left[\hbar v_F (\tau k_x \sigma_x - k_y \sigma_y) + \frac{E_g}{2} \sigma_z \right]
$$
$$
+ \sigma_- \otimes \left[\hbar v_F (\tau k_x \sigma_x + k_y \sigma_y) + \frac{E_g}{2} \sigma_z \right]
$$
$$
+ \sigma_x \otimes \sigma_x \gamma_1, \quad (19)
$$

where $\sigma_\pm = (I \pm \sigma_z)/2$ and $\hbar v_F = 3\gamma_0 a/2$, and, as before, $\mathbf{k} = (k_x, k_y)$ is a momentum measured relative to the Dirac points.

Diagonalizing this Hamiltonian, the following dispersion relation is found:

$$
E_{\mathbf{k}}^{\lambda,\eta} \approx \frac{\lambda}{2} \sqrt{E_g^2 + (2\gamma_1 + 3\eta\gamma_0 ak)^2}, \quad (20)
$$

with $\lambda = \pm 1$ or c/v depending on if it is used as a number or as an index, and $\eta = \pm 1$. As in the case of the AB bilayer, we see that the energy dispersion is independent of the valley index τ. The depiction of $E_{\mathbf{k}}^{\lambda,\eta}$ near the K point is given in Fig. 6. There, we see that the band structure of the AA′ bilayer presents a drastically different shape compared to that of the AB bilayer. While before we found that the two valence/conduction bands were clearly separated in energy, here we see that a critical point exists at $k = 0$ where the bands touch. Moreover, contrary to the AB bilayer, where the extrema of the bands were located at zero momentum, here we find the band maxima and minima at $k = 2\gamma_1/3\gamma_0 a$. The eigenvectors found from the diagonalization of the low-energy Hamiltonian are

$$
|u_{\mathbf{k}}^{v,\tau,\eta}\rangle = \frac{1}{\sqrt{\mathcal{V}_{\eta,\mathbf{k}}}} \begin{bmatrix} \frac{E_g - \sqrt{E_g^2 + 4(\gamma_1 + \eta \hbar v_F k)^2}}{2(\gamma_1 + \eta \hbar v_F k)} \\ \eta\tau e^{-i\tau\theta} \\ \eta\tau e^{-i\tau\theta} \frac{E_g - \sqrt{E_g^2 + 4(\gamma_1 + \eta \hbar v_F k)^2}}{2(\gamma_1 + \eta \hbar v_F k)} \\ 1 \end{bmatrix},
$$

$$|u_{\mathbf{k}}^{c,\tau,\eta}\rangle = \frac{1}{\sqrt{\mathcal{C}_{\eta,\mathbf{k}}}} \begin{bmatrix} \frac{E_g + \sqrt{E_g^2 + 4(\gamma_1 + \eta\hbar v_F k)^2}}{2(\gamma_1 + \eta\hbar v_F k)} \\ \eta\tau e^{-i\tau\theta} \\ \eta\tau e^{-i\tau\theta} \frac{E_g + \sqrt{E_g^2 + 4(\gamma_1 + \eta\hbar v_F k)^2}}{2(\gamma_1 + \eta\hbar v_F k)} \\ 1 \end{bmatrix}, \qquad (21)$$

where $\mathcal{C}_{\eta,\mathbf{k}}/\mathcal{V}_{\eta,\mathbf{k}}$ are normalization factors.

B. Excitons and conductivity

In order to obtain the excitonic energies and wave functions of the AA′ bilayer, one must return to the BSE, first presented in Eq. (8). Because in the previous section we already discussed the nuances of the BSE and outlined our approach to solving it, we do not repeat the same analysis here. Instead, we note only that the spinors given in Eq. (21) already have the phase choice which allows the transformation of the BSE, from a 2D integral equation to a 1D problem (see Appendix C for details on how to solve the 1D integral equation).

Considering a suspended bilayer ($\epsilon = 1$) and once again using $r_0 = 16$ Å [29], we solve the BSE and find the energies and wave functions of the excitons for the AA′ bilayer. We stress that similarly to the case of the AB configuration, when the BSE was solved, a corrected band gap of $E_g = 6.96$ eV was considered to match the value reported in Ref. [29]. Once again, the exact value of the band gap should not have a significant impact on the qualitative analysis of the results. As in the previous section, we solved the BSE using a 100-point Gauss-Legendre quadrature, which guaranteed the convergence of the excitonic energies and wave functions of the first 10 states.

In Figs. 7(a) and 7(b), we depict the wave functions $|\mathbf{\Psi}(k)|^2 = \sum_{cv} |\psi_{cv}(k)|^2$ of two of the states found by solving the BSE. These two states have energies $E_{n=1} = 5.64$ eV and $E_{n=2} = 6.36$ eV and correspond to the first two bright states of the system, i.e., the ones that originate the first resonances of the optical conductivity (shown below). We note that both of these states are doubly degenerate, without accounting for spin or valley degeneracy. For comparison, in [29], the first two peaks were predicted to appear at 5.35 and 6 eV, respectively. An exact match of the binding energies was not expected due to the different parametrizations of the band structure. However, as we shall see below, our results agree with those of Ref. [29] on the nature of the excitons behind these resonances. Analyzing the representation of the wave functions in momentum space, we realize that both resemble the wave functions of the s-states of the hydrogen atom since both are finite at the origin, and then decay to zero with zero and one nodes for the $n = 1$ and $n = 2$ states, respectively. Because of the unique band structure of the AA′ bilayer, and contrary to what we did in the AB configuration, here we cannot reduce the four-band problem to an approximate two-band one since it is impossible to define a pair of bands which could be considered the most relevant one for the low-energy response. Hence, the labeling of these states as s-states is based solely on their wave functions, in analogy with the hydrogen atom for which only s-states have finite wave functions at the origin.

In Figs. 7(c) and 7(d), we depict the wave function of the two states in real space when the hole is placed on the sublattice $|t, 2\rangle$ (corresponding to a nitrogen atom) and find
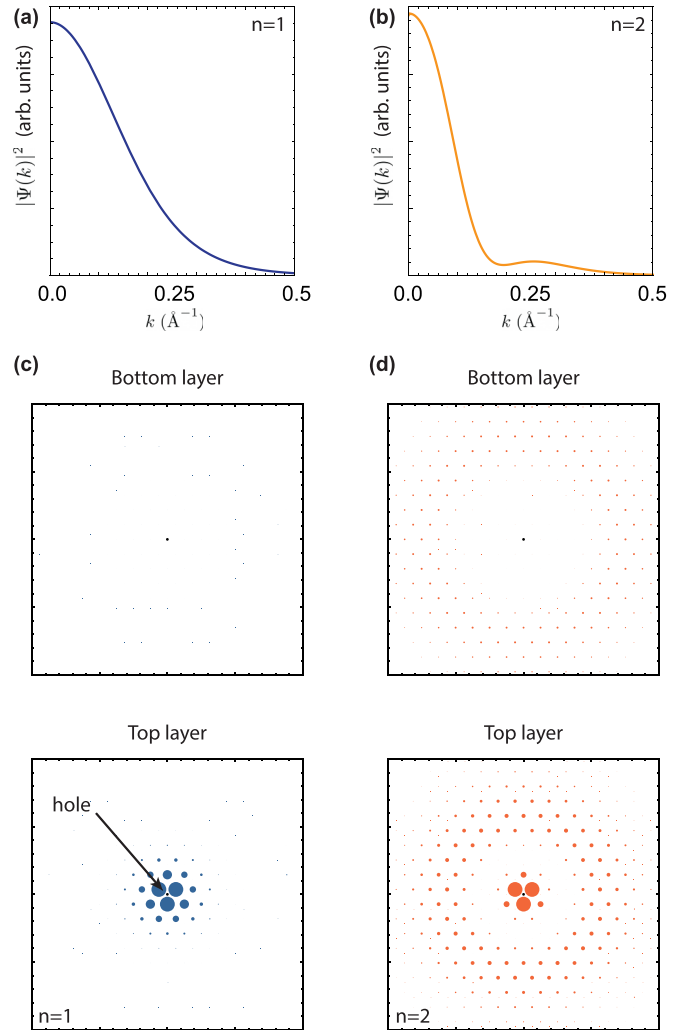

FIG. 7. (a),(b) Wave functions $|\mathbf{\Psi}(k)|^2 = \sum_{cv} |\psi_{cv}(k)|^2$ of the exciton states which are responsible for the first two resonances of the optical conductivity (highlighted in the same color as the respective wave function). (c),(d) Real-space representation of the absolute value of the wave function when the hole is placed in the $|t, 2\rangle$ sublattice (containing a nitrogen atom). The position of the hole is marked by a black dot.

that both are mostly intralayer excitons since the real-space wave function is mainly distributed over same layer where the hole is located. If the hole is placed on the sublattice $|b, 2\rangle$ (also a nitrogen atom), the results are identical to the ones depicted, only this time the wave function is almost entirely distributed over the bottom layer. When the hole is placed in either $|b/t, 1\rangle$ sublattices (with boron atoms), the resulting real-space wave function is essentially zero, indicating the preference of holes to appear on nitrogen atoms. These considerations are further backed by the values found when the wave function is integrated over each layer for a given position of the hole, which we show in Table II. The identification of these two states as being due to (mainly) intralayer s-excitons agrees with [29], where the same conclusion was obtained from *ab initio* calculations and symmetry considerations.

Now that the solutions of the BSE have been found, we can evaluate the longitudinal conductivity of the AA′ bilayer.

TABLE II. Integrate values of the square modulus of the sub-lattice resolved real-space wave function for the AA$'$ bilayer. The horizontal top row indicates the sublattice where the hole is placed, while the two columns on the left indicate the exciton, and the layer where the electron is located.

		$|1, b\rangle$	$|2, b\rangle$	$|1, t\rangle$	$|2, t\rangle$
$n = 1$	Bottom	0.01	0.46	0.00	0.02
	Top	0.00	0.02	0.01	0.46
$n = 2$	Bottom	0.01	0.33	0.00	0.14
	Top	0.00	0.14	0.01	0.33

Using the definition given in Eq. (12) for the conductivity, we obtain the result depicted in Fig. 8, where the area shaded in blue corresponds to the conductivity obtained accounting for 10 exciton states (once again, states with $m = \pm\tau$ are selected, only this time both present identical oscillator strengths.). The dark blue and orange outlines are the individual contributions of the two s-states whose wave functions were depicted in Fig. 7. First, we highlight the resemblance between our result and that of Ref. [29], especially for the first resonances, where we see that the location of the first two peaks, as well as their relative intensity, is similar in both works. At higher energies, however, we observe significant differences between our conductivity and the one obtained with *ab initio* calculations. This mismatch at higher energies was to be expected since ours is a low-energy theory, incapable of capturing the more nuanced features near the band edge. Nonetheless, the similarities at lower energies are a good indicator of the validity of our results. The conductivity of the AA$'$ bilayer resembles that of the monolayer [15] since in both cases the s-states are the bright one, and both present a set of resonances with monotonically decreasing oscillator strength. When compared to the conductivity of the AB bilayer, we find that the small
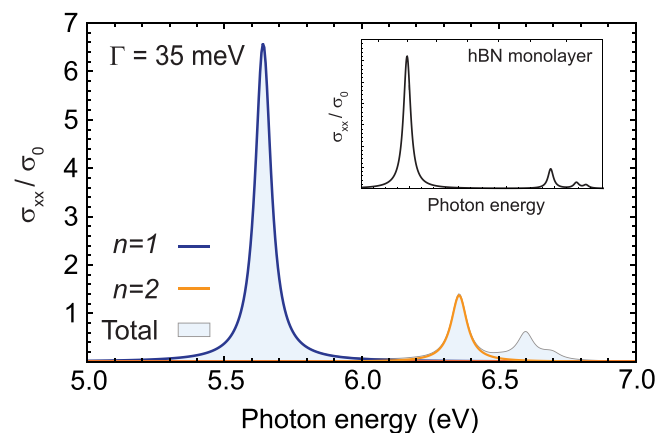

FIG. 8. Optical conductivity of an AA$'$ hBN bilayer accounting for the first 10 exciton states with $m = \pm\tau$ (the contributions from both valleys were accounted for). The first two resonances correspond to the excitonic states depicted in Fig. 8. To obtain this result, a phenomenological broadening of 35 meV was considered. The conductivity is given in terms of the conductivity of graphene, $\sigma_0 = e^2/4\hbar$. The inset shows a schematic depiction of the monolayer conductivity [15].
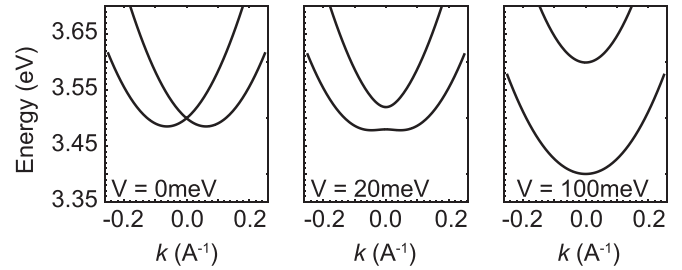

FIG. 9. Conduction bands of the biased AA$'$ bilayer, for three different bias values: $V = 0$, $V = 20$, and $V = 100$ meV. The valence bands present an identical dispersion relation.

peak between the first two resonances of Fig. 8 is absent in the AA$'$ configuration; hence, this small resonance can then be seen as a fingerprint of the AB stacking.

C. The effect of bias

One of the main features of the AA$'$ bilayer is its peculiar band structure, particularly the degeneracy at $k = 0$. An interesting thing to consider is the effect of lifting said degeneracy. To study this possibility, we now briefly consider the case of a biased AA$'$ bilayer. The bias can be introduced in the system through the application of a vertical displacement field. Since the application of such a field breaks the inversion symmetry of the AA$'$ bilayer, one may expect new optical selection rules for the biased bilayer when compared to the unbiased case.

To introduce the effect of bias in our low-energy model, we need only add a new contribution to the low-energy Hamiltonian given in Eq. (19),

$$H_{\text{bias}} = V I \otimes \sigma_z, \qquad (22)$$

with V quantifying the magnitude of the bias, I the identity matrix, and σ_z the z Pauli matrix. The bands associated with this new Hamiltonian are depicted in Fig. 9, where we see that for a small bias, the degeneracy at $k = 0$ is indeed lifted and the lower-energy conduction band acquires the form of a Mexican hat, similar to what is found in biased bilayer graphene. As the bias increases, so does the separation between the two bands and the shape of the bottom band becomes closer to a simple parabolic dispersion. We also note that although we only show the results for positive bias, the bands for negative bias are identical to the ones presented here.

Solving the BSE (using the same parameters that we used in the unbiased case) with this new Hamiltonian, and computing the conductivity due to an in-plane linearly polarized external electric field, we obtain the result depicted in Fig. 10, where different values for V are considered (the results for negative bias are identical). First, we see that, as expected, for zero bias the result of Fig. 8 is recovered. Then, as the bias increases, we observe that the first resonance is shifted to higher energies despite the reduction of the band gap, reflecting a reduction of its binding energy. Furthermore, we note that the initially simple features at higher energies become significantly more complex as the bias increases since different new small resonances start to appear. From the inspection of the real-space wave functions, we find that these new small
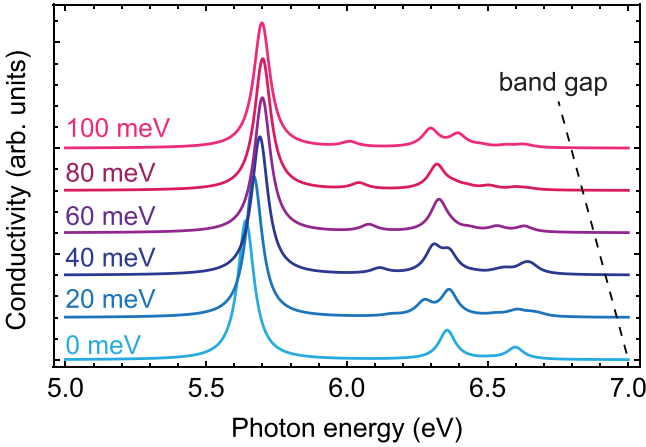
FIG. 10. Optical conductivity for the biased AA′ bilayer for different bias values. The results for negative bias are identical. The different conductivities are vertically shifted for clarity. Also depicted is the location of the band gap for each bias value.

resonances are associated with excitons which appear to be mainly interlayer (electron and hole in opposite layers). The excitons originating the larger resonances, which in the unbiased case were almost entirely intralayer, see their interlayer component increase. At last, we note that in the presence of external bias, the conductivity becomes more like the one found for the AB bilayer, which we assign to the breaking of inversion symmetry.

As we saw in Fig. 7, at zero bias, the resonances on the conductivity are essentially due to s-states, whose wave functions are finite at $k = 0$. However, as soon as some bias is introduced in the system, the symmetry of the problem changes and the optical selection rules are affected. Since for the biased bilayer we can split the bands into low-energy and high-energy groups, an approximate two-band model can be employed (see Sec. II D), allowing us to establish approximate optical selection rules. Applying the Lowdin partitioning, as described prior to Eq. (16), we find the following effective two-band Hamiltonian:

$$H_{\text{bias, eff}} = \begin{pmatrix} \Delta(-|V|) & -\frac{9\gamma_0^2\gamma_1\Delta(|V|)}{8V^3-2VE_g^2}k^2 \\ -\frac{9\gamma_0^2\gamma_1\Delta(|V|)}{8V^3-2VE_g^2}k^2 & -\Delta(-|V|) \end{pmatrix}, \quad (23)$$

where $\Delta(x) = \sqrt{(E_g/2 + x)^2 + \gamma_1^2}$. In its current form, this Hamiltonian holds for both $V > 0$ and $V < 0$ (but clearly fails to describe $V = 0$, the unbiased case). Using the procedure of Ref. [41] one more time, we identify the winding number as $w = 0$ and, as a consequence, the bright excitons are those with $m_X = \pm\tau$, that is, p-states. If trigonal warping had been considered, for example by including nonvertical interlayer hoppings, then states with $m = \pm 2$ and $m = \pm 4$ could also be excited (due to an additional factor of 3 stemming from the lattice symmetry contributing to m_X). Note how for the biased AA′ bilayer, the s-states are dark even if trigonal warping is considered, in stark contrast with the unbiased case, where s-states dominate the optical response.

IV. DISCUSSION

In this paper, we studied the optical conductivity due to the excitonic effects of two types of hBN bilayers: the AB and AA′ configurations. The comprehension of the properties of these bilayers is of great utility in the study of twisted bilayers at arbitrary angles since the results we presented correspond to the limit cases of 0° and 60° rotation.

To obtain the excitonic spectrum of each type of bilayer, we solved the Bethe-Salpeter equation (BSE) using the Bloch factors given by a low-energy four-band Hamiltonian. To ease the numerical weight of the calculation, we avoided the process of solving a 2D integral equation by a judicious choice of the phases of the Bloch factors, allowing us to cast the BSE into a 1D problem, which can then be solved in a rather efficient way. We emphasize that the method we presented to solve the four-band BSE gives better results than those of effective theories, such as the Lowdin partitioning. Although useful to extract optical selection rules, this type of effective approach fails to accurately predict the optical response (as we saw for the AB bilayer) and may even be impossible to apply (as we saw for the AA′ bilayer). Moreover, our approach is far less computationally expensive than methods which require the solution of the BSE in two dimensions, allowing the exploration of such systems by a broader audience.

Regarding the conductivities of the two considered bilayers, we found that the AB configuration presents an optical response where both intralayer and interlayer excitons participate. In particular, we found the first (and largest) excitonic resonance to be due to a mainly intralayer exciton, followed by a small, yet well-resolved resonance due to an interlayer exciton (which is only captured when the four bands of the model are accounted for); this small peak is followed by a larger one, also due to a mainly interlayer exciton. Furthermore, we found that for the AB bilayer, the two main resonances in the optical conductivity could be assigned with the hydrogenic label of p-states (angular quantum number equal to 1); f-states (angular quantum number 3) are also allowed to be excited, albeit with tiny oscillator strengths, and s-states (angular quantum number 0) appear if trigonal warping is accounted for.

For the AA′ bilayer, we found an optical conductivity dominated by mainly intralayer excitons, to which we assigned the hydrogenic label of s-states due to the line shape of the wave functions in momentum space, in agreement with [12]. Contrary to the AB stacking, the conductivity of the AA′ bilayer presented a set of resonances with monotonically decreasing magnitude (similar to the monolayer). Hence, the small peak between two larger ones in the AB bilayer is a clear differentiating feature between the two considered configurations.

When the case of a biased AA′ bilayer was studied, we found that the s-states became dark and the p-states dominated the optical spectrum; the change of optical selection rules is a consequence of the symmetry breaking introduced by the bias. Moreover, as the bias increased, we found that the first (and more pronounced) resonance was shifted to higher energies, going against the trend of the band gap, which decreased with increasing bias. We also found that the introduction of the bias led to an overall more complex optical response due to the increased contribution from interlayer excitons.

APPENDIX A: DETAILS ON THE DFT CALCULATIONS

Density functional theory (DFT) calculations were performed using the software package QUANTUM ESPRESSO [44]. We used a scalar-relativistic norm-conserving pseudopotential [45,46] and the generalized gradient approximation of Perdew-Burke-Ernzerhof (GGA-PBE) [47]. The plane-wave cutoff was 80 Ry and, for the integration over the Brillouin zone, the scheme proposed by Monkhorst-Pack [48] with a grid of $18 \times 18 \times 1 \mathbf{k}$ points was used. A vacuum size between the layer images of 25 bohr was enough to avoid interactions between the periodic images. We also included the van der Waals correction proposed by Grimme [49,50]. Atoms were relaxed to establish the spacing between layers. The tight-binding parameters were obtained by fitting the DFT bands along a path in the first Brillouin zone, as depicted in Fig. 11. Only the valence bands were fitted since the DFT calculations less accurately capture the empty states of the conduction bands [19].

APPENDIX B: ON THE EXCITON'S ANGULAR QUANTUM NUMBER

1. Two-band system

Let us start by considering the problem of an hBN monolayer, which we take as a concrete example of a two-band
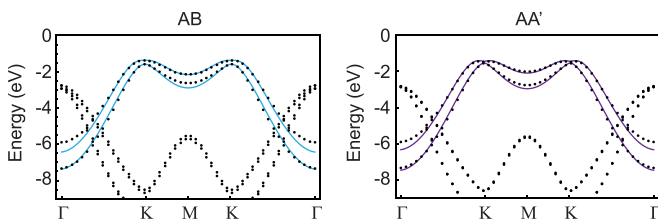

FIG. 11. Fit of the tight-binding bands to the results found from DFT calculations. For the AB bilayer, we find $E_g = 4.585$ eV, $\gamma_0 = 2.502$ eV, and $\gamma_1 = 0.892$ eV. For the AA′ bilayer, we obtain $E_g = 4.650$ eV, $\gamma_0 = 2.491$ eV, and $\gamma_1 = 0.595$ eV.

system [15]. We model the monolayer with a two-band Dirac Hamiltonian to describe its low-energy electronic properties. From the diagonalization of the Hamiltonian, one easily shows that the Bloch factors take the form [14]

$$|u_{c,\mathbf{k}}\rangle = [e^{i\theta} \sin \xi_k, \cos \xi_k]^{\mathrm{T}}, \quad \text{(B1)}$$

$$|u_{v,\mathbf{k}}\rangle = [e^{i\theta} \cos \xi_k, -\sin \xi_k]^{\mathrm{T}}, \quad \text{(B2)}$$

where c/v labels the conduction/valence band, $\theta = \arctan k_y/k_x$, and ξ_k is a function which approaches zero as the momentum k vanishes. Alternatively, we could have defined the Bloch factors as

$$|w_{c,\mathbf{k}}\rangle = [e^{i\theta} \sin \xi_k, \cos \xi_k]^{\mathrm{T}}, \quad \text{(B3)}$$

$$|w_{v,\mathbf{k}}\rangle = [\cos \xi_k, -e^{-i\theta} \sin \xi_k]^{\mathrm{T}}, \quad \text{(B4)}$$

since state vectors are only defined up to a global phase factor.

Let us now introduce excitons in this system. We consider that as in the main text, the wave function of an exciton in momentum space can be written as $\psi_{cv}(\mathbf{k}) = f_{cv}(k)e^{im\theta}$. The real-space wave function can be defined as

$$\Psi^u_{\alpha\beta}(\mathbf{r}_e, \mathbf{r}_h) = \sum_{\mathbf{k}} e^{i(\mathbf{K}+\mathbf{k})\cdot(\mathbf{r}_e-\mathbf{r}_h)} f_{cv}(k)e^{im_u\theta} u^\alpha_{\mathbf{k},c}(u^\beta_{\mathbf{k},v})^*, \quad \text{(B5)}$$

$$\Psi^w_{\alpha\beta}(\mathbf{r}_e, \mathbf{r}_h) = \sum_{\mathbf{k}} e^{i(\mathbf{K}+\mathbf{k})\cdot(\mathbf{r}_e-\mathbf{r}_h)} f_{cv}(k)e^{im_w\theta} w^\alpha_{\mathbf{k},c}(w^\beta_{\mathbf{k},v})^*, \quad \text{(B6)}$$

where $\mathbf{r}_e$ and $\mathbf{r}_h$ are the electron and hole positions, respectively, and $u/w^\alpha_{\mathbf{k},c}$ refers to the α sublattice entry of the Bloch factor $|u/w_{\mathbf{k},c}\rangle$ (an analogous definition holds for $u/w^\beta_{\mathbf{k},v}$). From the definition of the Bloch factors and recalling that $\lim_{k\to 0} \xi_k = 0$, we see that the product $u^\alpha_{\mathbf{k},c}(u^\beta_{\mathbf{k},v})^*$ approximately introduces a phase $e^{-i\theta}$ in the definition of the wave function, while $w^\alpha_{\mathbf{k},c}(w^\beta_{\mathbf{k},v})^*$ introduces no phase. Hence, when we define the wave function with the u-Bloch factors, we find a pseudospin angular quantum number of $m^{\mathrm{ps}}_u = -1$, while for the w-Bloch factors, we have $m^{\mathrm{ps}}_w = 0$. Notice how we focused our analysis near $k = 0$ since that is where selection rules are stronger; momentum dependence tends to weaken optical selection rules.

For a linearly polarized electric field, one can show that the optical response is proportional to $\Omega^x_{u/w} = \sum_{\mathbf{k}} \psi_{cv}(\mathbf{k})\langle u/w_{v,\mathbf{k}}|x|u/w_{c,\mathbf{k}}\rangle$ [39,41]. Like we did in the main text, the matrix element of the position operator can be found from the commutator of the Hamiltonian with the position operator itself. As we said in the beginning, we are considering a Dirac Hamiltonian to model the system. Because of that, we can write $\Omega_{u/w}$ as

$$\Omega^x_u \propto \sum_{\mathbf{k}} f_{cv}(k)e^{im_u\theta} \frac{\langle u_{v,\mathbf{k}}|\sigma_x|u_{c,\mathbf{k}}\rangle}{E_{v,k} - E_{c,k}}, \quad \text{(B7)}$$

$$\Omega^x_w \propto \sum_{\mathbf{k}} f_{cv}(k)e^{im_w\theta} \frac{\langle w_{v,\mathbf{k}}|\sigma_x|w_{c,\mathbf{k}}\rangle}{E_{v,k} - E_{c,k}}, \quad \text{(B8)}$$

with $E_{v/c,k}$ the dispersion relations of the model Hamiltonian, which obviously independent of the phase choice for the Bloch factors. Converting the sum over $\mathbf{k}$ into a 2D integral in momentum space and carrying out the necessary calculations, one finds that Ω_u and Ω_w are only finite if $m_u = \pm 1$

and $m_w = 0, -2$, respectively. Thus, at first, it may appear that the choice of phase for the Bloch factors changes the optical selection rules since different angular dependencies for the exciton envelope function are selected. However, when the contribution of the pseudospin angular quantum number is taken into account, we see that $m_u + m_u^{ps} = m_w + m_w^{ps} = 0, -2$. The sum of these two contributions is independent of the phase chosen for the Bloch factors and is the appropriate angular quantum number [38].

2. Four-band system

In the first part of this Appendix, we saw how to define the appropriate angular quantum number for a two-band system such as an hBN monolayer. To achieve this, one must sum the angular quantum number from the excitonic envelope function with the angular quantum number given by the Bloch factors to obtain the appropriate angular quantum number; while the first two depend on the phase chosen for the Bloch factors, the last one is independent of it (as it should be, in order to be an approximately good quantum number).

Let us now consider a four-band model, such as the ones treated in the main text. For such a system, the real-space exciton wave function reads

$$\Psi_{\alpha,\beta}(\mathbf{r}_e, \mathbf{r}_h) = \sum_{\mathbf{k},c,v} e^{i(\mathbf{K}+\mathbf{k})\cdot(\mathbf{r}_e-\mathbf{r}_h)} f_{cv}(k)e^{im\theta} u_{\mathbf{k},c}^{\alpha} \left(u_{\mathbf{k},v}^{\beta}\right)^*, \quad \text{(B9)}$$

which differs from the definition given in the first part of this Appendix due to the sums over the bands. The problem in defining an angular quantum number for the exciton in a four-band system lies in the definition of the pseudospin contribution. While the contribution from the envelope function to the angular quantum number is still well defined, the same cannot be said for the the pseudospin part since, in principle, each of the terms $|u_{c,\mathbf{k}}\rangle\langle u_{v,\mathbf{k}}|$ can contribute with a different complex exponential (which is the case for the two systems treated in the main text), thus stopping us from obtaining a well-defined m_{ps}, with which the appropriate angular quantum number of the exciton (independent of phase choices) could be determined. Although this could be bypassed with a phase choice that, for example, left all the spinors without complex exponentials in the $k \to 0$ limit, that would not be helpful for our approach, where a specific phase choice has to be performed to cast the BSE into a 1D problem, thus simplifying its numerical solution.

APPENDIX C: SOLVING THE BSE

In this Appendix, we shall give a more in-depth description of how to numerically solve the Bethe-Salpeter equation (BSE) presented in the main text. The method we present is an extension of the one applied for the hydrogen atom in Ref. [40]. We take Eq. (10) of the main text as our starting point:

$$\left(E_k^c - E_k^v\right)f_{cv}(k) - \sum_{c'v'}\int q\,dq\,d\theta_q V(\mathbf{k} - \mathbf{q})\langle u_{\mathbf{k}}^c|u_{\mathbf{q}}^{c'}\rangle\langle u_{\mathbf{q}}^{v'}|u_{\mathbf{k}}^v\rangle f_{c'v'}(q)e^{im(\theta_q - \theta_k)} = Ef_{cv}(k). \quad \text{(C1)}$$

As discussed in the main text, we consider the spinor product to have the following form:

$$\langle u_{\mathbf{k}}^c|u_{\mathbf{q}}^{c'}\rangle\langle u_{\mathbf{q}}^{v'}|u_{\mathbf{k}}^v\rangle = \sum_{\lambda}\mathcal{A}_{\lambda}^{cc'vv'}(k,q)e^{i\lambda(\theta_q - \theta_k)}, \quad \text{(C2)}$$

where λ is some integer, and $\mathcal{A}_{\lambda}^{cc'vv'}(k,q)$ are coefficients determined by the explicit computation of the spinor product. Inserting this into the previous equation, and noting that $V(\mathbf{k} - \mathbf{q}) \equiv V(k,q,\theta_q - \theta_k)$, one finds

$$\left(E_k^c - E_k^v\right)f_{cv}(k) - \sum_{c'v'}\sum_{\lambda}\int q\,dq\,d\vartheta V(k,q,\vartheta)\mathcal{A}_{\lambda}^{cc'vv'}(k,q)f_{c'v'}(q)e^{i(m+\lambda)\vartheta} = Ef_{cv}(k), \quad \text{(C3)}$$

where we introduced the variable change $d\theta_q \to d\vartheta$ with $\vartheta = \theta_q - \theta_k$. Now, recalling the definition of $V(k,q,\vartheta)$, we introduce a new function, $\mathcal{I}_\nu(k,q)$, which corresponds to the integral over $d\vartheta$, that is,

$$\mathcal{I}_\nu(k,q) = \int_0^{2\pi}\frac{\cos(\nu\vartheta)}{\kappa(k,q,\vartheta)[1 + r_0\kappa(k,q,\vartheta)]}d\vartheta, \quad \text{(C4)}$$

with $\kappa(k,q,\vartheta) = \sqrt{k^2 + q^2 - 2kq\cos\vartheta}$. Notice how only $\cos(\nu\theta)$ enters the integral since the analogous term in $\sin(\nu\vartheta)$ vanishes by symmetry. From inspection, it should be clear that when $q = k$, the function $\mathcal{I}_\nu(k,q)$ is numerically ill behaved and, as such, must be treated carefully. Looking at its definition, one sees that we can express $\mathcal{I}_\nu(k,q)$ in terms of partial fractions as

$$\mathcal{I}_\nu(k,q) = \int_0^{2\pi}\frac{\cos(\nu\vartheta)}{\kappa(k,q,\vartheta)}d\vartheta - r_0\int_0^{2\pi}\frac{\cos(\nu\vartheta)}{[1 + r_0\kappa(k,q,\vartheta)]}d\vartheta \quad \text{(C5)}$$

$$\equiv \mathcal{J}_\nu(k,q) - \mathcal{K}_\nu(k,q), \quad \text{(C6)}$$

where from these two terms only the first one, $\mathcal{J}_\nu(k,q)$, is problematic when $k = q$ since $\mathcal{K}_\nu(k,q)$ contains an additional 1 in the denominator which prevents any divergence. Before we explain how to avoid this numerical problem, let us first express the

BSE in a more convenient manner. First, we write

$$\left(E_k^c - E_k^v\right)f_{cv}(k) - \sum_{c'v'}\sum_{\lambda}\int_0^{\infty}\left\{\mathcal{J}_{m+\lambda}(k,q)\mathcal{A}_{\lambda}^{cc'vv'}(k,q)f_{c'v'}(q) - \mathcal{K}_{m+\lambda}(k,q)\mathcal{A}_{\lambda}^{cc'vv'}(k,q)f_{c'v'}(q)\right\}qdq = Ef_{cv}(k). \tag{C7}$$

Then, we define $\mathcal{B}_m^{cc'vv'}(k,q) = \sum_{\lambda}\mathcal{J}_{m+\lambda}(k,q)\mathcal{A}_{\lambda}^{cc'vv'}(k,q)$ and $\mathcal{C}_m^{cc'vv'}(k,q) = \sum_{\lambda}\mathcal{K}_{m+\lambda}(k,q)\mathcal{A}_{\lambda}^{cc'vv'}(k,q)$. With these new definitions, one finds

$$\left(E_k^c - E_k^v\right)f_{cv}(k) - \sum_{c'v'}\int_0^{\infty}\mathcal{B}_m^{cc'vv'}(k,q)f_{c'v'}(q)qdq + \sum_{c'v'}\int_0^{\infty}\mathcal{C}_m^{cc'vv'}(k,q)f_{c'v'}(q)qdq = Ef_{cv}(k). \tag{C8}$$

Now, let us focus on the numerical problem associated with $\mathcal{B}_m^{cc'vv'}(k,q)$. To treat the divergence that appears when $k = q$, we introduce an auxiliary function $g_m(k,q)$ and introduce the modification

$$\int_0^{\infty}\mathcal{B}_m^{cc'vv'}(k,q)f_{c'v'}(q)qdq \rightarrow \int_0^{\infty}\left[\mathcal{B}_m^{cc'vv'}(k,q)f_{c'v'}(q) - g_m(k,q)f_{c'v'}(k)\right]qdq + f_{c'v'}(k)\int_0^{\infty}g_m(k,q)qdq, \tag{C9}$$

with g_m defined in such a way that $\lim_{q\to k}[\mathcal{B}_m^{cc'vv'}(k,q) - g_m(k,q)] = 0$. Following Ref. [40], we define g_m as

$$g_m = \mathcal{B}_m^{cc'vv'}(k,q)\frac{2k^2}{k^2+q^2}. \tag{C10}$$

With the analytical part of the calculation taken care of, we shall now discuss how to numerically solve the equation we have arrived to. To achieve this, we first introduce a variable change which transforms the improper integral over $[0,\infty)$ into one with finite integration limits, such as $[0,1]$; with this goal in mind, we introduce $q = \tan[\pi x/2]$. Afterwards, we discretize the variables k and x (and, consequently, q), and find

$$\left(E_{k_i}^c - E_{k_i}^v\right)f_{cv}(k_i) + \sum_{c'v'}\sum_{j=1}^N\mathcal{C}_m^{cc'vv'}(k_i,q_j)f_{c'v'}(q_j)q_j\frac{dq}{dx_j}$$

$$- \sum_{c'v'}\sum_{j\neq i}\mathcal{B}_m^{cc'vv'}(k_i,q_j)f_{c'v'}(q_j)q_j\frac{dq}{dx_j}w_j - f_{c'v'}(k_i)\left\{\int_0^{\infty}g_m(k_i,p)pdp - \sum_{j\neq i}g_m(k_i,q_j)q_j\frac{dq}{dx_j}\right\} = Ef_{cv}(k_i), \tag{C11}$$

where N is the number of points and w_j is the weight function of the chosen numerical quadrature; also, $q_j \equiv q(x_j)$ and $dq/dx_j \equiv [dq/dx]_{x=x_j}$. Furthermore, we note that $\int_0^{\infty}g_m(k_i,p)pdp$ is numerically well behaved as opposed to the original integral, $\int_0^{\infty}\mathcal{B}_m^{cc'vv'}(k_i,p)pdp$. Regarding the choice of quadrature, we employ a Gauss-Legendre quadrature, which is defined as [51]

$$\int_a^b f(y)dy \approx \sum_{i=1}^N w_i f(y_i), \tag{C12}$$

where

$$y_i = \frac{a+b+(b-a)\xi_i}{2}, \tag{C13}$$

with ξ_i the ith zero of the Legendre polynomial $P_N(y)$, and

$$w_i = \frac{b-a}{(1-\xi_i)^2[P_N'(\xi_i)]^2}, \tag{C14}$$

with $P_N'(\xi_i) \equiv [dP_N(y)/dy]_{y=\xi_i}$.

At last, the only thing left to do is to realize that this equation can be expressed as an eigenvalue problem of a $4N \times 4N$ matrix. This matrix can be thought of as a 4×4 matrix of matrices, each one with dimensions $N \times N$. The 16 blocks come from the different combinations of the indexes c, c', v, and v', with each block corresponding to a $N \times N$ matrix stemming from the numerical discretization of the integral. Solving the eigenvalue problem, one finds the exciton energies and wave functions.

[1] J. D. Caldwell, I. Aharonovich, G. Cassabois, J. H. Edgar, B. Gil, and D. Basov, Nat. Rev. Mater. **4**, 552 (2019).

[2] G. Wang, A. Chernikov, M. M. Glazov, T. F. Heinz, X. Marie, T. Amand, and B. Urbaszek, Rev. Mod. Phys. **90**, 021001 (2018).

[3] C. R. Dean, A. F. Young, I. Meric, C. Lee, L. Wang, S. Sorgenfrei, K. Watanabe, T. Taniguchi, P. Kim, K. L. Shepard, and J. Hone, Nat. Nanotechnol. **5**, 722 (2010).

[4] A. Kretinin, Y. Cao, J. Tu, G. Yu, R. Jalil, K. Novoselov, S. Haigh, A. Gholinia, A. Mishchenko, M. Lozada, T. Georgiu, C. Woods, F. Withers, P. Blake, G. Eda, A. Wirsig, C. Hucho, K.

Watanabe, T. Taniguchi, A. Geim *et al.*, Nano Lett. **14**, 3270 (2014).

[5] M. Ashhadi, M. Hadavi, and Z. Sarri, Phys. E **87**, 312 (2017).

[6] I. Epstein, A. J. Chaves, D. A. Rhodes, B. Frank, K. Watanabe, T. Taniguchi, H. Giessen, J. C. Hone, N. M. Peres, and F. H. Koppens, 2D Mater. **7**, 035031 (2020).

[7] P. Cudazzo, I. V. Tokatly, and A. Rubio, Phys. Rev. B **84**, 085406 (2011).

[8] K. Watanabe, T. Taniguchi, and H. Kanda, Nat. Mater. **3**, 404 (2004).

[9] Y. Kubota, K. Watanabe, O. Tsuda, and T. Taniguchi, Science **317**, 932 (2007).

[10] F. Fuchs, C. Rödl, A. Schleife, and F. Bechstedt, Phys. Rev. B **78**, 085103 (2008).

[11] H.-P. Komsa and A. V. Krasheninnikov, Phys. Rev. B **88**, 085318 (2013).

[12] T. Galvani, F. Paleari, H. P. C. Miranda, A. Molina-Sánchez, L. Wirtz, S. Latil, H. Amara, and F. Ducastelle, Phys. Rev. B **94**, 125303 (2016).

[13] S. Di Sabatino, J. Berger, and P. Romaniello, Faraday Discuss. **224**, 467 (2020).

[14] A. Taghizadeh and T. G. Pedersen, Phys. Rev. B **99**, 235433 (2019).

[15] J. C. G. Henriques, G. B. Ventura, C. D. M. Fernandes, and N. M. R. Peres, J. Phys.: Condens. Matter **32**, 025304 (2020).

[16] R. Ditchfield, W. Hehre, and J. Pople, J. Chem. Phys. **52**, 5001 (1970).

[17] C. Zhang, H. Wang, W. Chan, C. Manolatou, and F. Rana, Phys. Rev. B **89**, 205436 (2014).

[18] M. F. M. Quintela and N. M. Peres, Eur. Phys. J. B **93**, 1 (2020).

[19] R. M. Ribeiro and N. M. R. Peres, Phys. Rev. B **83**, 235312 (2011).

[20] Y. Fujimoto and S. Saito, Phys. Rev. B **94**, 245427 (2016).

[21] D. Wickramaratne, L. Weston, and C. G. Van de Walle, J. Phys. Chem. C **122**, 25524 (2018).

[22] J. M. B. Lopes dos Santos, N. M. R. Peres, and A. H. Castro Neto, Phys. Rev. Lett. **99**, 256802 (2007).

[23] J. M. B. Lopes dos Santos, N. M. R. Peres, and A. H. Castro Neto, Phys. Rev. B **86**, 155449 (2012).

[24] L. Xian, D. M. Kennes, N. Tancogne-Dejean, M. Altarelli, and A. Rubio, Nano Lett. **19**, 4934 (2019).

[25] N. R. Walet and F. Guinea, Phys. Rev. B **103**, 125427 (2021).

[26] K. Yao, N. R. Finney, J. Zhang, S. L. Moore, L. Xian, N. Tancogne-Dejean, F. Liu, J. Ardelean, X. Xu, D. Halbertal *et al.*, Sci. Adv. **7**, eabe8691 (2021).

[27] W. Aggoune, C. Cocchi, D. Nabok, K. Rezouali, M. A. Belkhir, and C. Draxl, Phys. Rev. B **97**, 241114(R) (2018).

[28] C. Attaccalite, M. Grüning, H. Amara, S. Latil, and F. Ducastelle, Phys. Rev. B **98**, 165126 (2018).

[29] F. Paleari, T. Galvani, H. Amara, F. Ducastelle, A. Molina-Sánchez, and L. Wirtz, 2D Mater. **5**, 045017 (2018).

[30] K. Mengle and E. Kioupakis, APL Mater. **7**, 021106 (2019).

[31] Y. Suzuki and K. Watanabe, Phys. Chem. Chem. Phys. **22**, 2908 (2020).

[32] I. Paradisanos, S. Shree, A. George, N. Leisgang, C. Robert, K. Watanabe, T. Taniguchi, R. J. Warburton, A. Turchanin, X. Marie, I. C. Gerber, and B. Urbaszek, Nat. Commun. **11**, 2391 (2020).

[33] T. G. Pedersen, Phys. Rev. B **92**, 235432 (2015).

[34] K. S. Thygesen, 2D Mater. **4**, 022004 (2017).

[35] N. S. Rytova, Moscow Univ. Phys. Bull. **22**, 3 (1967).

[36] L. Keldysh, JETP Lett. **29**, 658 (1979).

[37] T. Tian, D. Scullion, D. Hughes, L. H. Li, C.-J. Shih, J. Coleman, M. Chhowalla, and E. J. Santos, Nano Lett. **20**, 841 (2020).

[38] C.-H. Park and S. G. Louie, Nano Lett. **10**, 426 (2010).

[39] T. Cao, M. Wu, and S. G. Louie, Phys. Rev. Lett. **120**, 087402 (2018).

[40] C. Yi-Ping Chao and S. L. Chuang, Phys. Rev. B **43**, 6530 (1991).

[41] X. Zhang, W.-Y. Shan, and D. Xiao, Phys. Rev. Lett. **120**, 077401 (2018).

[42] P.-O. Löwdin, J. Chem. Phys. **19**, 1396 (1951).

[43] R. Winkler, S. Papadakis, E. De Poortere, and M. Shayegan, *Spin-Orbit Coupling in Two-Dimensional Electron and Hole Systems*, Vol. 41 (Springer-Verlag, Berlin, Heidelberg, 2003).

[44] P. Giannozzi, S. Baroni, N. Bonini, M. Calandra, R. Car, C. Cavazzoni, D. Ceresoli, G. L. Chiarotti, M. Cococcioni, I. Dabo, A. Dal Corso, S. de Gironcoli, S. Fabris, G. Fratesi, R. Gebauer, U. Gerstmann, C. Gougoussis, A. Kokalj, M. Lazzeri, L. Martin-Samos *et al.*, J. Phys.: Condens. Matter **21**, 395502 (2009).

[45] D. R. Hamann, Phys. Rev. B **88**, 085117 (2013).

[46] M. Schlipf and F. Gygi, Comput. Phys. Commun. **196**, 36 (2015).

[47] J. P. Perdew, K. Burke, and M. Ernzerhof, Phys. Rev. Lett. **77**, 3865 (1996).

[48] H. J. Monkhorst and J. D. Pack, Phys. Rev. B **13**, 5188 (1976).

[49] S. Grimme, J. Comput. Chem. **27**, 1787 (2006).

[50] V. Barone, M. Casarin, D. Forrer, M. Pavone, M. Sambi, and A. Vittadini, J. Comput. Chem. **30**, 934 (2009).

[51] P. Kythe and P. Puri, *Computational Methods for Linear Integral Equations* (Birkhäuser, Boston, 2002).